

High Yield Solution Growth of FACsPbBr₃ Single Crystals with Low Defect Density for Gamma-ray Spectroscopy

Jinsong Huang (✉ jhuang@unc.edu)

University of North Carolina at Chapel Hill <https://orcid.org/0000-0002-0509-8778>

Liang Zhao

University of North Carolina at Chapel Hill

Ying Zhou

University of North Carolina at Chapel Hill

Zhifang Shi

University of North Carolina at Chapel Hill <https://orcid.org/0000-0003-1673-0983>

Zhenyi Ni

University of North Carolina at Chapel Hill

Ye Liu

University of North Carolina at Chapel Hill

Article

Keywords: Perovskite crystals, radiation detectors, solution method, high stability, high yield

Posted Date: March 23rd, 2022

DOI: <https://doi.org/10.21203/rs.3.rs-1428730/v1>

License: © ⓘ This work is licensed under a Creative Commons Attribution 4.0 International License.

[Read Full License](#)

High Yield Solution Growth of FACsPbBr₃ Single Crystals with Low Defect Density for Gamma-ray Spectroscopy

Liang Zhao¹, Ying Zhou¹, Zhifang Shi¹, Zhenyi Ni¹, Ye Liu¹, and Jinsong Huang^{1,2*}

¹Department of Applied Physical Sciences, University of North Carolina at Chapel Hill, USA

²Department of Chemistry, University of North Carolina at Chapel Hill, USA

Abstract: Metal halide perovskites are promising candidates for room temperature gamma-ray spectrum detectors, however, it is challenging to grow high-quality single crystals under operation conditions to make them economically competitive to existing materials. Here, we report the growth of centimeter-size formamidinium-cesium lead bromide (FACsPbBr₃) single crystals at high yield from low purity (98%) and thus low-cost precursors using a relatively low-temperature solution method. The introduction of FA into CsPbBr₃ reduces defect density in crystals by eliminating the phase transition during the cooling from the growth temperature to room temperature, which significantly improves the yield of crack-free and low trap density crystals. As-grown FACsPbBr₃ exhibits a high resistivity of $9.5 \times 10^9 \Omega \text{ cm}$, balanced hole and electron mobility-lifetime products of $(2.2\text{-}3.2) \times 10^{-3} \text{ cm}^2 \text{ V}^{-1}$, a long charge recombination lifetime of 182 ns, and a record low deep trap density of $5.6 \times 10^{10} \text{ cm}^{-3}$, which eventually results in a high charge collection efficiency of 84% under gamma-ray. The FACsPbBr₃ spectrum detectors with an asymmetrical metal electrode configuration have achieved an energy resolution of 2.9% for 662 keV ¹³⁷Cs γ -rays. The improved spectrum capability allows them to resolve Pb K _{α,β} X-rays (75-85 keV) for the first time in ¹³⁷Cs spectrum. FACsPbBr₃ single crystals show excellent stability under large biases up to 1000 volts, and no degradation of spectrum performance after 7 months.

Key words: Perovskite crystals, radiation detectors, solution method, high stability, high yield

Room-temperature semiconductor radiation detectors with high performance and low cost have broad applications in medical imaging, homeland security, scientific research, and industrial material inspection¹. Gamma-ray (γ -ray) spectral detectors have many demanding requirements

for the semiconductor materials, such as high stopping power, high mobility-lifetime ($\mu\tau$) products for efficient charge collection, large resistivity to reduce noise, low trap density to avoid charge trapping, and low cost for scalable fabrication². After decades of research, less than a handful of room temperature semiconductors have been identified which have good spectral detection capability, including $\text{Cd}_x\text{Zn}_{1-x}\text{Te}$ (CZT)^{3,4}, TlBr ⁵, and HgI_2 ⁶. Nevertheless, these materials still face some limitations that prevent their broad applications. For example, TlBr and HgI_2 struggle with the charging polarization effect and stability issues^{5,6}, and spectral-grade CZT single crystals are still too expensive ($\sim\$2,000/\text{cm}^3$)⁷, caused by expensive Bridgeman growth methods and related purification processes. Metal halide perovskites (MHPs), which have made impressive progress in applications of solar cells⁸, light emitting diodes (LEDs)⁹, and photodetectors¹⁰, are rising as promising candidates for room-temperature radiation detectors. Their high mass density and large atomic number elements (Pb, I, Br...) result in a large stopping power of MHPs comparable to that of CZT¹¹. MHP single crystals have been demonstrated to have large $\mu\tau$ products, unique defect tolerance, relatively large bandgap, and near intrinsic conduction, which makes them promising candidates for room temperature γ -ray spectral detectors¹²⁻¹⁸. Most important of all, high-quality MHP crystals can be synthesized by versatile low-cost solution methods in large throughput¹⁹, which offers an opportunity to significantly reduce the crystal material costs and custom designing of materials with different form factors.

Gamma-ray spectral detectors have been demonstrated using several perovskite compositions, including doping-compensated methylammonium lead tribromide ($\text{MAPbBr}_{2.94}\text{Cl}_{0.06}$)¹², methylammonium lead triiodide (MAPbI_3)¹⁴, and all-inorganic cesium lead tribromide (CsPbBr_3)¹⁵. Among all MHPs studied in the past few years, CsPbBr_3 grown using Bridgeman method has been demonstrated to have the best energy resolution of 1.4% for ^{137}Cs 662 keV γ -ray¹³. CsPbBr_3 has much better thermal and chemical stability than MA-based perovskites, and is particularly very stable under high bias, despite of the slightly lower $\mu\tau$ products than other MHPs, which enables their good spectral response. However, CsPbBr_3 single crystals grown from expensive high-purity precursor materials (99.999%) might not be cost-competitive to replace CZT, which also need expensive crystal purification after crystal growth¹³. To reduce the cost of the CsPbBr_3 crystals, we explored solution methods to grow CsPbBr_3 single crystals^{20,21}, and discovered that an inner salt additive of 3-(Decyldimethylammonio) propanesulfonate inner salt (DPSI)²² could assist the growth of cuboidal shape, very transparent CsPbBr_3 single crystals

which otherwise would be needle shape due to the unbalanced growth speed along different facets. Although we managed to find some good crystals which showed an energy resolution of 5.5%, the yield of high-quality CsPbBr₃ single crystals was extremely low (less than 5%)²⁰. The low crystal product yield can be attributed to the phase transition of CsPbBr₃ crystals when they were cooled down from growth temperature to room temperature. CsPbBr₃ has a cubic structure (Pm $\bar{3}$ m) at temperatures above 130 °C, tetragonal structure (P4/mbm) at 88-130 °C, and orthorhombic structure (Pbnm) at room temperature²³. Although we avoided the cubic to tetragonal phase transition by controlling the growth temperature to be 80-120 °C, the phase transition from tetragonal to orthorhombic was inevitable which induces a large residual stress and causes the formation of many twins and cracks²⁰. This phase transition significantly limited the yield of high-quality crystals.

In this article, we report solution-grown formamidinium-cesium lead bromide (FA_xCs_{1-x}PbBr₃, 0<x<1) single crystals with excellent γ -ray spectral performance. We find the stress from phase transition not only causes visible extended defects but also increases the density point defects in the single crystals. Using a cation alloy, we found that FA-rich FA_xCs_{1-x}PbBr₃ crystals could maintain the cubic phase above room temperature, avoiding the phase transition and improving the crystal quality and yield. It significantly reduced the defect density in the mixed cation FA_xCs_{1-x}PbBr₃ single crystals and improved the spectral response.

We first studied the influence of the phase transition induced internal stress on the structural and electronic property of CsPbBr₃ single crystals. We generally observed very few or no cracks on CsPbBr₃ single crystals during crystal growth stage, as shown by a typical photo in **Fig. S1a**. The crystals in solution are very transparent. However, after we picked up the as-grown crystals from the hot solution, many cracks appeared when they were cooled down to room temperature, as shown in **Fig. 1a**. In addition, we observed parallel domain structure in CsPbBr₃ single crystals, which are most likely twin boundaries (**Fig. S1b**), indicating the presence of residual strain from phase transitions that needs to be released¹⁵. We deposited small, pixelated metal electrodes at different locations of one crystal with cracks to investigate device leakage current, as shown in **Fig. 1b**. Pixel #1 is free of visible crack, while pixel #2, and #3 are right on top of the cracks. As shown in **Fig. 1c**, it is not surprising that these cracks did result in a much larger leakage current with a dark current density of $\sim 10^5$ nA cm⁻² under 100 V, corresponding to

a very small bulk resistivity of $\sim 10^6 \Omega \text{ cm}$. However, crack-free pixel #1 surprisingly also had a large dark current density of $\sim 10^4 \text{ nA cm}^{-2}$ and thus a low resistivity of $\sim 10^7 \Omega \text{ cm}$. Despite that it is better than the locations with cracks, this resistivity is still far lower than what a spectroscopic grade crystal needs to have (10^9 - $10^{11} \Omega \text{ cm}$ for CZT crystals). This indicates that the stress from the phase transition not only causes visible cracks that affect local crystal quality, but also generates many invisible point defects which dramatically increase the leakage current of the devices. The larger leakage current can be explained by the unintentional doping of these perovskites by the defects. The presence of cracks in the crystals can be an indicator for the degree of internal stress, providing a simple way to screen crystals by visual inspection. Thus, avoiding phase transition during crystal synthesis and device fabrication should be considered to reduce defect generation and improve device performance.

To avoid the phase transition between the growth temperature and application temperature, we chose FAPbBr₃ to alloy with CsPbBr₃ to form FA_xCs_{1-x}PbBr₃ mixed cation crystals with a cubic structure shown in **Fig. 1d**. FAPbBr₃ has a similar stopping power to γ -ray (0.1-1 MeV) with CZT and CsPbBr₃, as shown in **Fig S2**. In contrast to CsPbBr₃, FAPbBr₃ crystals keep the cubic phase at temperatures above -2 °C, which makes it free of phase transition between crystal growth temperature (~ 60 °C) and room temperature. A previously constructed FAPbBr₃-CsPbBr₃ binary phase diagram shows that FA-rich FA_xCs_{1-x}PbBr₃ crystals can maintain cubic phase at room temperature when Cs percentage is less than $\sim 30\%$ ²⁴, as shown in **Fig 1e**. We grew a series of FA_xCs_{1-x}PbBr₃ single crystals with various compositions using the additive assisted solution growth method. FAPbBr₃ and CsPbBr₃ precursors were mixed at different ratios. DPSI was added as an additive to reduce defect density. Tiny seed crystals (diameter <1 mm) were placed at bottle of fresh and stable mixed precursor solution for the big crystal growth. The growth temperature and solvent evaporation were carefully controlled to avoid multiple crystal growth. The addition of more FA into the precursors also increased the crystal growth speed, as summarized by **Fig. 1f**, thanks to the much higher solubility of FAPbBr₃ in the common solvents. Centimeter-sized FA-rich FA_xCs_{1-x}PbBr₃ crystals can be grown from solution within ten days. The photos of the as-synthesized crystals FA_xCs_{1-x}PbBr₃ with different Cs ratios are shown in **Fig. 1g**. As expected, CsPbBr₃ and Cs-richer FA_xCs_{1-x}PbBr₃ crystals showed lots of cracks and twin boundaries inside the crystals, while FA-richer FA_xCs_{1-x}PbBr₃ crystals are much clearer and have less cracks. The

color of the crystals changed with the precursor ratio, indicating a successful alloying of the mixed cation perovskites.

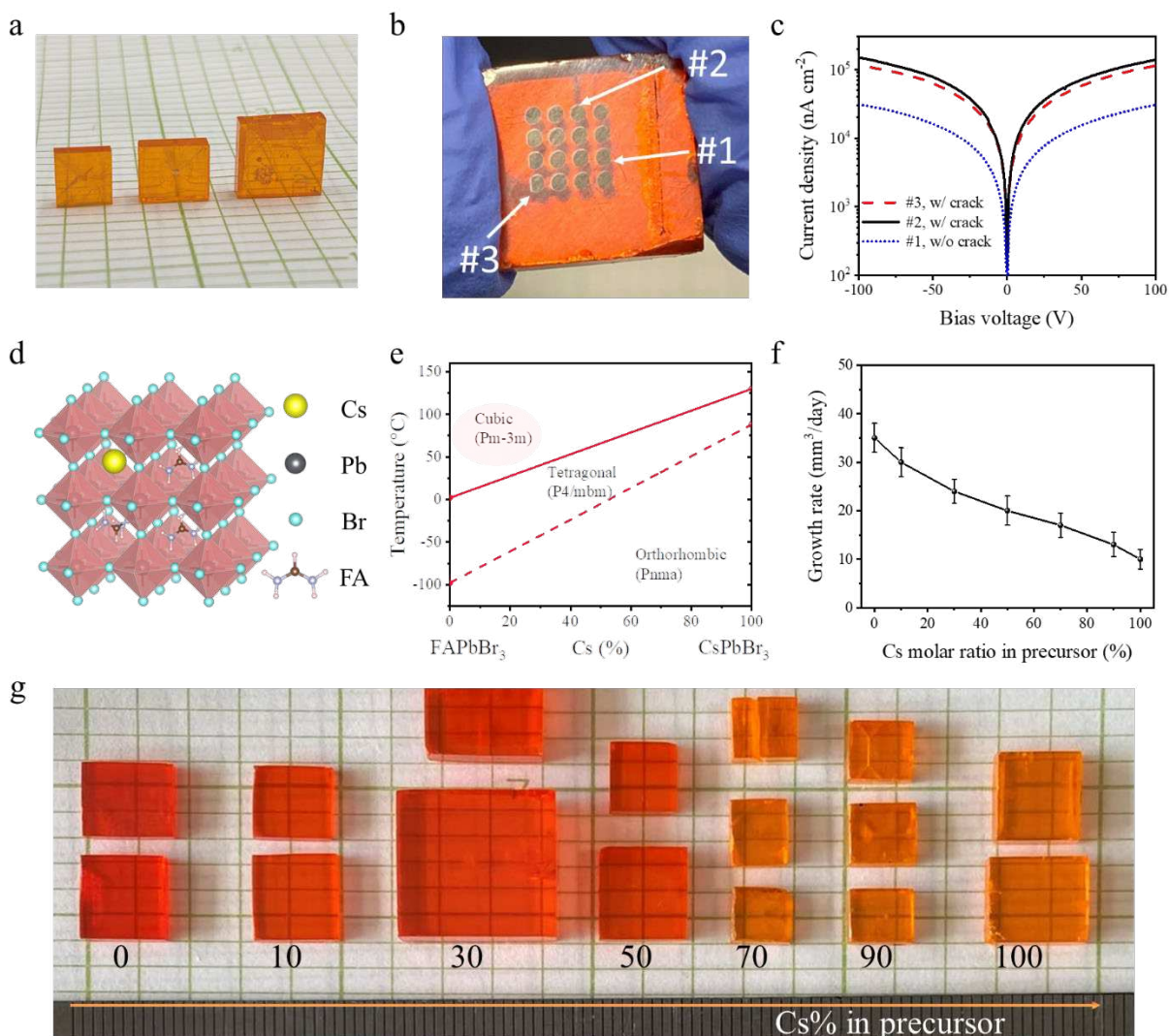


Fig. 1 Phase transition and growth of $\text{FA}_x\text{Cs}_{1-x}\text{PbBr}_3$ single crystals. **a**, Solution grown CsPbBr_3 single crystals with cracks. **b**, Pixel electrodes on a CsPbBr_3 crystal with visible cracks. **c**, Dark current densities of the different pixels on the CsPbBr_3 crystal with cracks. **d**, Crystal structure of $\text{FA}_x\text{Cs}_{1-x}\text{PbBr}_3$ single crystals with a cubic phase. **e**, Phase diagram of $\text{FA}_x\text{Cs}_{1-x}\text{PbBr}_3$. **f**, $\text{FA}_x\text{Cs}_{1-x}\text{PbBr}_3$ crystal growth speed at different Cs molar ratio in the precursor solution. **g**, A photo of several as-grown $\text{FA}_x\text{Cs}_{1-x}\text{PbBr}_3$ single crystals from different precursor solutions with varied Cs/(Cs+FA) ratio from 0% to 100%.

X-ray diffraction (XRD) measurement was performed to test $\text{FA}_x\text{Cs}_{1-x}\text{PbBr}_3$ crystallinity, lattice constant, and crystal structure at room temperature. As shown in **Fig. 2a**, all the diffraction peaks gradually shifted to larger diffraction angles when the Cs molar ratio in the precursor solution was increased from 10% to 90%, implying that Cs incorporated into the crystal lattice. These XRD patterns show that FA-rich precursors generate cubic-phase crystals and Cs-rich precursors prefer to form crystals with tetragonal or orthorhombic structure, as indicated by the split diffraction peaks. The actual compositions of these crystals were estimated based on the shift of the (002), (112) and (110) diffraction peaks according to Vegard's law by assuming a linear relationship of the lattice constant with the Cs ratio in the perovskites²⁵. As shown in **Fig. 2b**, the actual Cs incorporation ratio is slightly more than the Cs ratio in the precursor solution, because Cs solubility maybe lower than FA in the precursor solution. In addition, the photoluminescence (PL) emission peaks of $\text{FA}_x\text{Cs}_{1-x}\text{PbBr}_3$ single crystals are monotonously blue-shifted with increased Cs molar ratio in the crystals (**Fig. 2c**), which indicates a continuous bandgap changing. The calculated bandgap of $\text{FA}_x\text{Cs}_{1-x}\text{PbBr}_3$ single crystals has almost a linear relationship with the calculated Cs ratio in the perovskites, as shown in **Fig. 2d**. Composition uniformity is important in mixed composition crystals. We test XRD and PL spectra at different locations at one crystal, as shown in **Fig. S3**. The positions of XRD diffraction peaks and PL emission peaks keep the same, which demonstrates good composition uniformity.

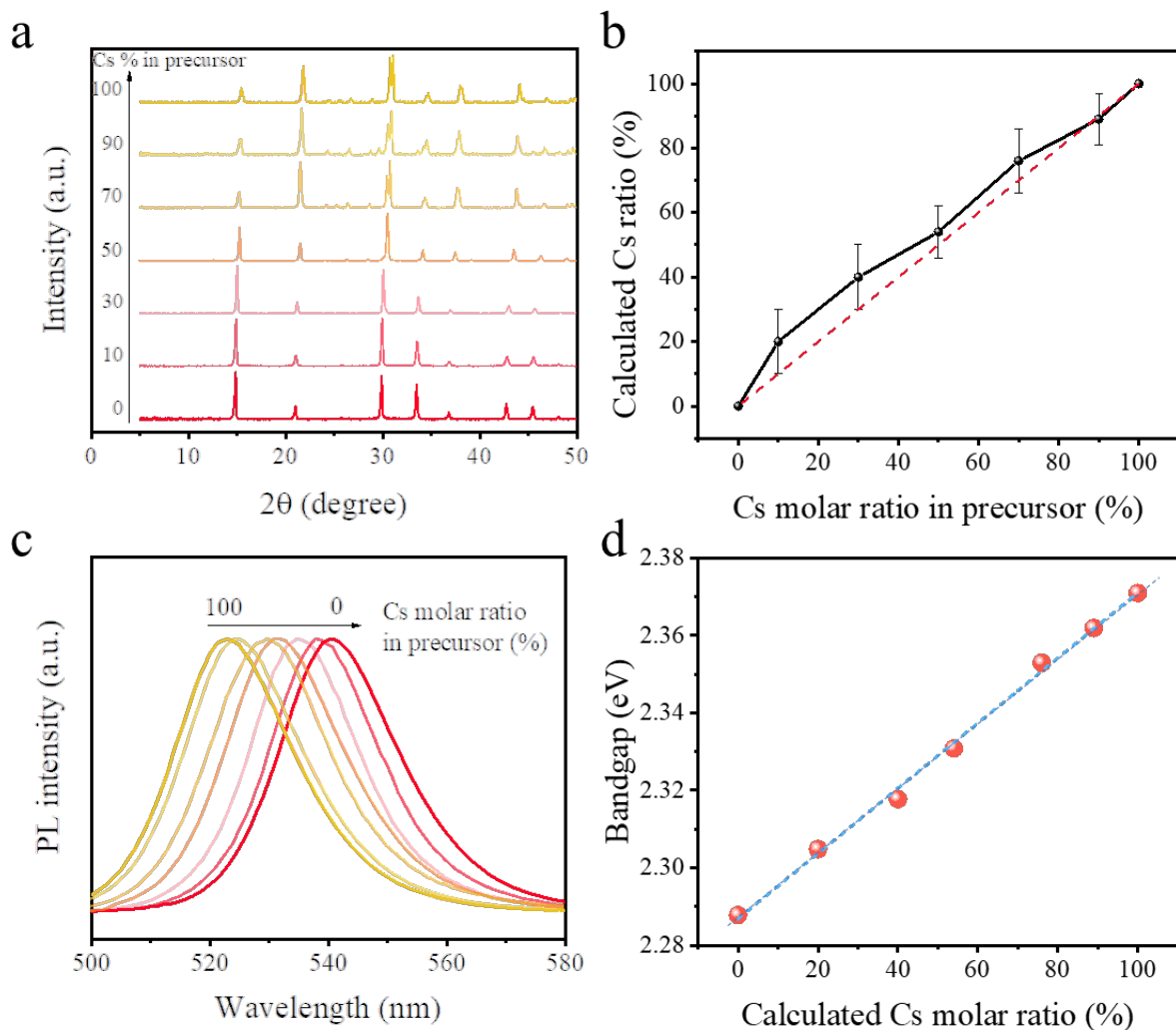


Fig. 2 Crystal structure and bandgap of $\text{FA}_x\text{Cs}_{1-x}\text{PbBr}_3$ crystals. **a** XRD spectra of $\text{FA}_x\text{Cs}_{1-x}\text{PbBr}_3$ single crystal powder. **b** the precursor composition ratio versus the calculated composition ratio. **c** photoluminescence (PL) measurement on $\text{FA}_x\text{Cs}_{1-x}\text{PbBr}_3$ crystals. **D.** Relationship of the $\text{FA}_x\text{Cs}_{1-x}\text{PbBr}_3$ optical bandgaps with the Cs molar ratio, where the optical bandgap was calculated from PL emission peaks, and Cs ratio was determined by lattice constant.

To determine a suitable composition for further study, we assessed crystal quality based on crystal appearance, resistivity, and trap density. **Fig. 3a** shows the resistivity of the $\text{FA}_x\text{Cs}_{1-x}\text{PbBr}_3$ single crystals grown with different precursor ratio. Au electrodes were deposited on both sides of these crystals by thermal evaporation, and I - V curves were measured in the dark. The crack-free $\text{FA}_{0.9}\text{Cs}_{0.1}\text{PbBr}_3$ shows the highest resistivity of $9.5 \times 10^9 \Omega \text{ cm}$, which is close to the best

commercial CZT materials. High resistivity enables extremely low noise during long period measurement even under a large voltage. We also observe that the FA-rich $\text{FA}_{0.9}\text{Cs}_{0.1}\text{PbBr}_3$ crystals have lowest chance to form cracks and very good transparency, as shown by the photo in **Fig.3b**, which implies higher yield of crystal growth and lower manufacturing costs. This confirms the elimination of stress can improve the crystal quality by reducing the point defect density and the associated self-doping. It is noted that some point defects may cause deep charge traps²⁶⁻²⁸.

The reduced internal stress is also expected to reduce the deep trap density in the $\text{FA}_{0.9}\text{Cs}_{0.1}\text{PbBr}_3$ single crystals. To evaluate the deep trap density in the bulk of crystals, we applied the drive-level capacitance profiling (DLCP) technique which can distinguish the bulk trap density from surface ones²⁹. The depth-dependent trap densities can be obtained by changing the depletion region into the crystal interior by applied bias so that the bulk trap density is evaluated. Here we evaluated the traps of FAPbBr_3 , $\text{FA}_{0.9}\text{Cs}_{0.1}\text{PbBr}_3$, and CsPbBr_3 with a depth smaller than 0.44 eV. These crystals were all grown by the same methods while the only difference is the precursor ratio. As shown in **Fig. 3c**, the $\text{FA}_{0.9}\text{Cs}_{0.1}\text{PbBr}_3$ crystal shows a record low trap density of $\sim 5.6 \times 10^{10} \text{ cm}^{-3}$, while CsPbBr_3 and FAPbBr_3 crystals have much higher trap density of $\sim 1.3 \times 10^{12} \text{ cm}^{-3}$ and $\sim 1.4 \times 10^{11} \text{ cm}^{-3}$, respectively. The ~ 20 times larger trap density in CsPbBr_3 can be explained by the stress induced defects, such as point defects (Br_{Pb} , Pb_{Br} , Pb_{i} ...) ³⁰, dislocations, and so on. It is to our surprise that FAPbBr_3 crystals still have twice trap density of $\text{FA}_{0.9}\text{Cs}_{0.1}\text{PbBr}_3$, despite of the absence of phase transition in this composition as well. It may be related to the incorporation of Cs may further reduce the trap density. We conducted time-resolved photoluminescence (TRPL) measurement to characterize the charge recombination of these crystals with different compositions. $\text{FA}_{0.9}\text{Cs}_{0.1}\text{PbBr}_3$ crystals showed a much longer charge recombination lifetime of $\sim 182 \text{ ns}$ than CsPbBr_3 ($\sim 5 \text{ ns}$), as shown in **Fig. 3d**. Although the TRPL lifetime is more an indication of crystal surface quality, it is also impacted by the crystal bulk charge recombination process. A much longer TRPL lifetime supports the lower trap density in $\text{FA}_{0.9}\text{Cs}_{0.1}\text{PbBr}_3$ crystals. After evaluating crystal quality from different aspects, we found $\text{FA}_{0.9}\text{Cs}_{0.1}\text{PbBr}_3$ crystals have the best quality among all the solution grown $\text{FA}_x\text{Cs}_{1-x}\text{PbBr}_3$ crystals, and thus detectors were fabricated with crystals of this composition for further device performance evaluation.

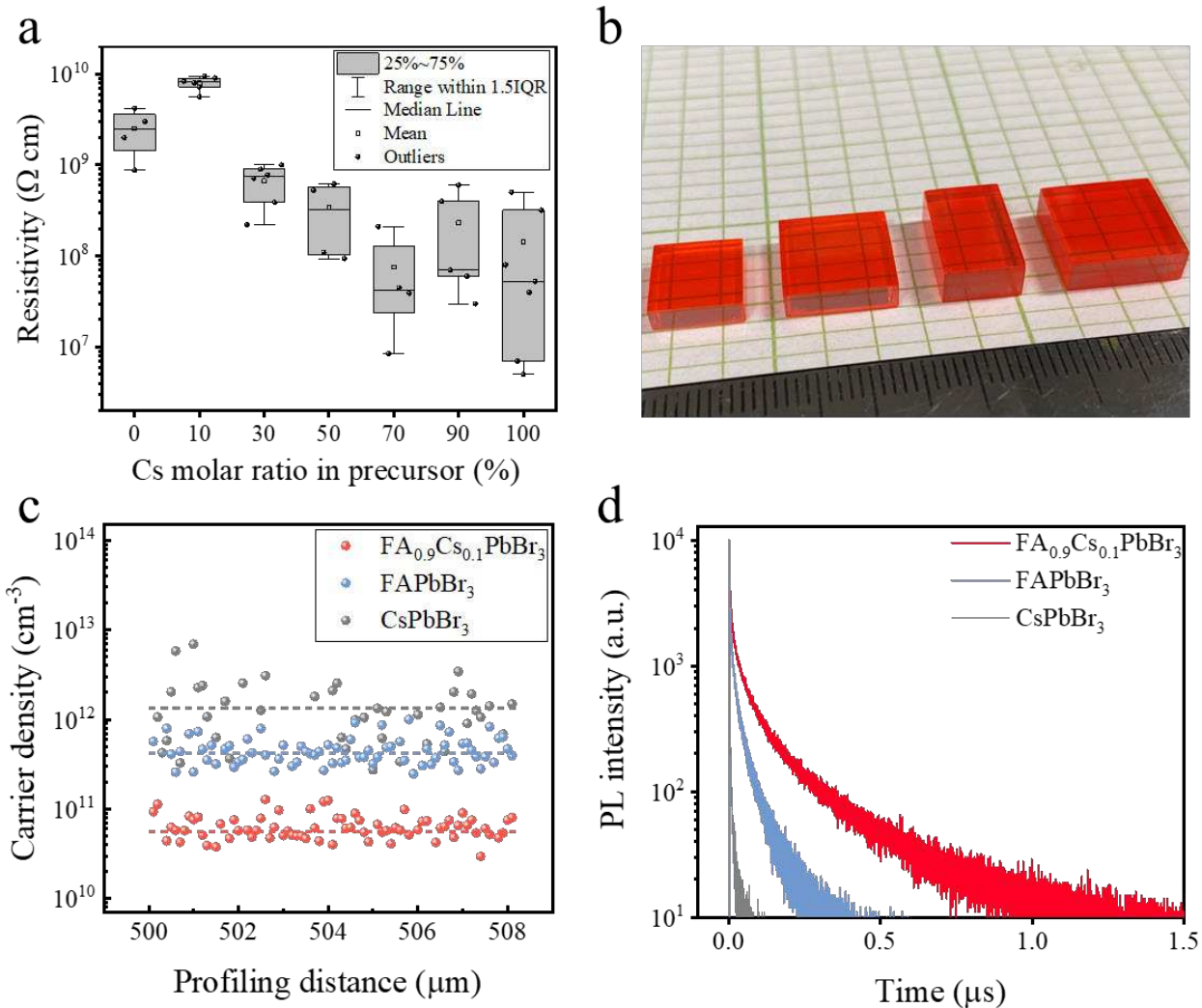


Fig. 3 FA_xCS_{1-x}PbBr₃ crystal quality evaluation, **a**, The resistivity of FA_xCS_{1-x}PbBr₃ single crystals grown from solution with different Cs molar ratios. **b**. A photo of as-grown optimized FA_{0.9}CS_{0.1}PbBr₃ crystals **c**. Bulk charge trap density measured by DLCP, where a large bias was applied to extend the depletion region into the bulk of the crystals. **d**. Charge recombination lifetime measured by time-resolved photoluminescence.

To test γ -ray spectral performance of devices, FA_{0.9}CS_{0.1}PbBr₃ detector was exposed to radiation from ¹³⁷Cs, ⁵⁷Co, and ²⁴¹Am radioactive isotopes, respectively. The detectors employed an asymmetrical metal electrode configuration using gold (Au) and bismuth (Bi) as anode and cathode, respectively, to reduce device noise. These metals do not notably react with

FA_{0.9}CS_{0.1}PbBr₃¹³. The negative bias was applied on the Au electrode while the Bi electrode is grounded. As shown in **Fig. S4**, the devices with Au as both electrodes showed a symmetric J-V curve, while replacing one of the two Au electrodes with Bi induced an obvious rectification of the dark current, indicating Au forms ohmic contact with FA_{0.9}CS_{0.1}PbBr₃. **Fig. 4a-b** show well-defined spectra with an energy resolution of 2.9% at 662 keV, and 5.9% at 122 keV, representing the best spectral resolution achieved by solution-grown MHP crystals. The full energy ¹³⁷Cs spectrum clearly showed photopeak (662 keV), Pb escape peak, Compton edge, backscatter peak, and Pb K_{α,β} X-rays (75-85 keV). It is the first time that this low energy peak was observed MHP crystals, which should be ascribed to very low device noise. The well-resolved ⁵⁷Co spectrum also showed many details, including the Pb X-ray escape peak (47 keV) and another γ -ray photopeak at 136 keV. FA_{0.9}CS_{0.1}PbBr₃ detector also can clearly resolve ²⁴¹Am spectrum with a resolution of 9.8±0.4 % at 59.5 keV (**Fig. S5a**), which is four times better than previously reported results of FAPbBr₃ single crystals³¹. FA_{0.9}CS_{0.1}PbBr₃ detectors showed a great linear response in the studied energy range from 59.5 to 662 keV. We calibrated the acquired γ -ray spectrum based on the ⁵⁷Co photopeak position at 122 keV¹⁵, then obtained the measured energy of ¹³⁷Cs 662 keV and ²⁴¹Am 59.5 keV γ -ray photopeaks. The device response to these different γ -ray sources has excellent linearity (>0.99), as shown in **Fig. 4c and Fig.S6**.

The polarization effect caused by ion migration and charge trapping is one major concern for some MHPs for radiation detection³², which results in spectrum shift and resolution degradation. The FA_{0.9}CS_{0.1}PbBr₃ detector has outstanding stability of the γ -ray response at room temperature under a large bias. During a continuous testing for 21 mins. under -1000 V, the count rate, peak channel number and resolution for a detector under ⁵⁷Co γ -ray were almost unchanged, as shown in **Fig 4d-e**, which demonstrate the excellent stability of this material under large bias and γ -ray. The extremely low trap density and defect-tolerance nature of solution-grown FA_{0.9}CS_{0.1}PbBr₃ crystals may suppress this detrimental polarization effect. Dark current drift is another indicator of ion migration for perovskites under large bias¹². FA_{0.9}CS_{0.1}PbBr₃ showed superior dark current stability with only ~1% of dark current drift for the device biased at -200 V for 2 hours (**Fig. S7**). In addition, FA_{0.9}CS_{0.1}PbBr₃ detectors demonstrated great long-term shelf stability. After 7-month storage, FA_{0.9}CS_{0.1}PbBr₃ detector still can acquire the ⁵⁷Co γ -ray spectrum with the same resolution as shown in **Fig. 4f**, which implies no degradation of devices. Impressive

operation and storage stability make $\text{FA}_{0.9}\text{Cs}_{0.1}\text{PbBr}_3$ a promising radiation detection semiconductor at room temperature.

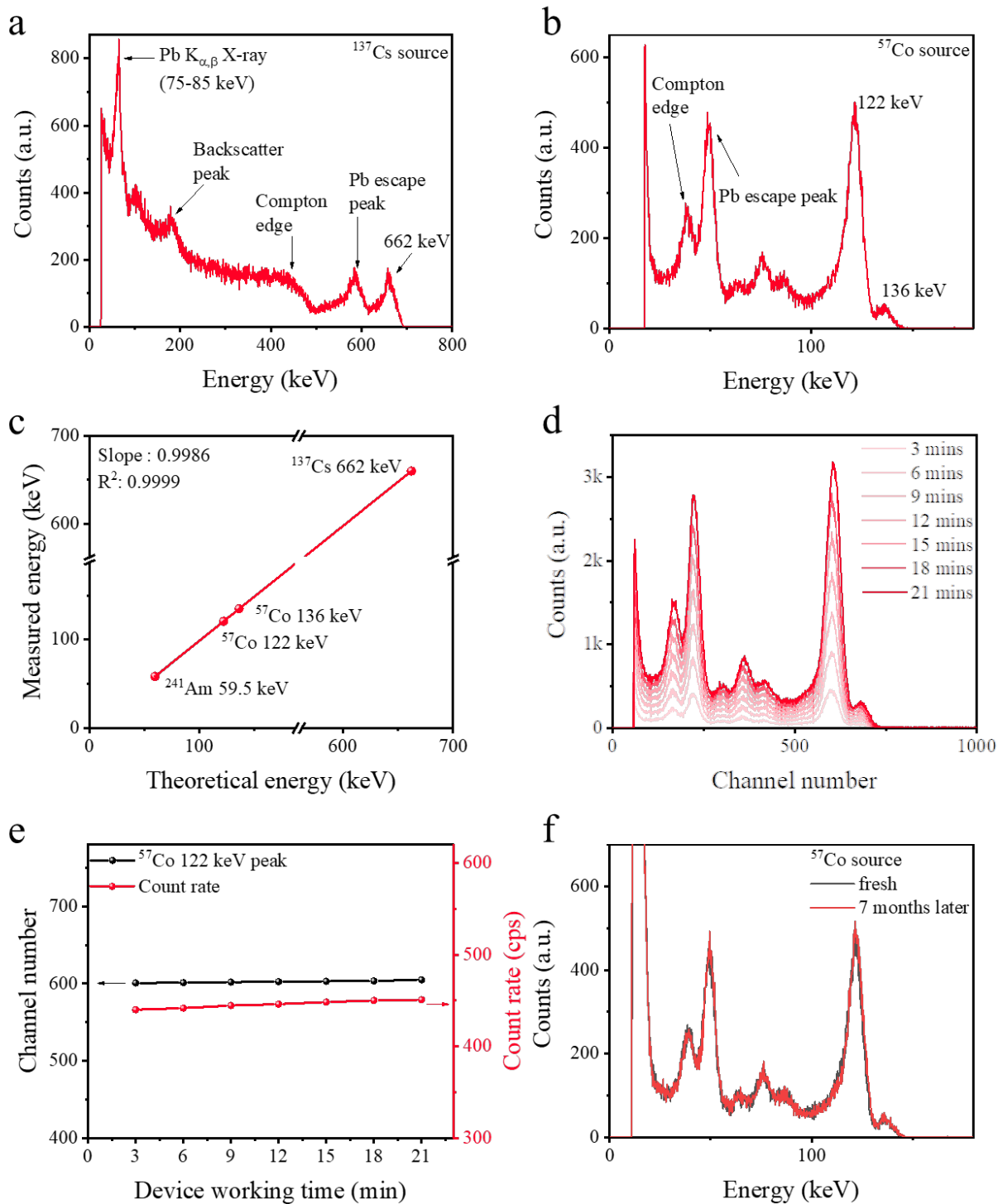


Fig. 4 Spectral response of FA_{0.9}Cs_{0.1}PbBr₃ detectors to different γ -ray sources. **a** Energy-resolved spectrum of ¹³⁷Cs γ -ray source with the 662 keV photopeak with a shaping time of 1 μ s. **b**, Energy-resolved spectrum of ⁵⁷Co γ -ray source with 122 keV and 136 keV photopeaks with a shaping time of 1 μ s. **c**, Detection response of FA_{0.9}Cs_{0.1}PbBr₃ devices to different γ -ray sources. **d** Spectrum shape, **e** the channel number of ⁵⁷Co 122 keV photopeak and count rate from the spectrum testing of FACsPbBr₃ devices biased at -1000 V for 21 mins under ⁵⁷Co γ -ray, **f** spectrum collected for the fresh device and after seven-month storage.

To understand the excellent detection performance of the FA_{0.9}Cs_{0.1}PbBr₃ devices, we characterized the electronic properties. Mobility-lifetime ($\mu\tau$) product is an essential parameter to evaluate charge collection efficiency (CCE) of radiation detector materials³³. To calculate the $\mu\tau$ product of FA_{0.9}Cs_{0.1}PbBr₃, we fitted different photopeak positions of ⁵⁷Co 122 keV under various biases by the modified Hecht equation¹³, where the electron and hole collections were distinguished by changing the polarity of the applied bias, as shown in **Fig. S8**. The derived hole and electron mobility-lifetime products are $3.2 \times 10^{-3} \text{ cm}^2 \text{ V}^{-1}$ and $2.2 \times 10^{-3} \text{ cm}^2 \text{ V}^{-1}$, respectively, as shown in **Fig. 5a**. We also used X-ray induced current scanning method to derive mobility-lifetime product. For this measurement, we put a lead slit on the side of the crystals, then moved the slit from anode to cathode, as illustrated in **Fig. S9a-c**. It directly shows that both electrons and holes can be collected, and a hole to electron mobility-lifetime product ratio of ~ 1.4 is derived from the voltage dependent current at cathode and anode, which is very closed to that derived from ⁵⁷Co photopeak positions. The electron mobility-lifetime product is slight lower than that of holes but they are pretty balanced, and these values are comparable to the best reported ones from CsPbBr₃ crystals grown by Bridgeman method. We estimated the CCE according to the collected charge numbers induced by 662 keV gamma ray. As shown in **Fig. S10**, the channel number of 662 keV photopeak is 1517, and the calculated channel number if all the charges can be collected is 1810. The CCE of the FA_{0.9}Cs_{0.1}PbBr₃ device is as high as 84%, which should be ascribed to the reduction of the traps in the single crystals.

Since FA_{0.9}Cs_{0.1}PbBr₃ devices can detect α -particle generated by ²⁴¹Am decay with an energy resolution of $17.5 \pm 0.9\%$ (**Fig. S5b**), we also extracted peak positions of 5.5 MeV radiation from voltage-dependent spectrums and fitted them by Hecht equation^{31,34}. The $\mu_h\tau_h$ and $\mu_e\tau_e$ are

$2.9 \times 10^{-3} \text{ cm}^2 \text{ V}^{-1}$ and $1.8 \times 10^{-3} \text{ cm}^2 \text{ V}^{-1}$, respectively, as shown in **Fig. S11** and **Fig. 5b**, which agree with those calculated from ^{57}Co photopeak positions. The incident 5.5 MeV α -particle can penetrate $\text{FA}_{0.9}\text{Cs}_{0.1}\text{PbBr}_3$ with a mean depth of $\sim 25.9 \text{ }\mu\text{m}$, which is calculated by SRIM software³⁵. This penetration depth is much smaller than the crystal thickness ($\sim 2.5 \text{ mm}$), so only one type of charges transport in the devices under α -particle irradiation. We applied the time-of-flight (ToF) technique to acquire charge carrier drift time t_t under different applied biases^{12,34}. **Fig. S12** shows the typical rising time (10-90% of signal intensity) under the bias ranging from 50-400 V for electron and hole collection. The hole and electron drift mobilities in $\text{FA}_{0.9}\text{Cs}_{0.1}\text{PbBr}_3$ crystals were calculated from the transit time and crystal thickness with known bias to be $262 \pm 7 \text{ cm}^2 \text{ V}^{-1} \text{ s}^{-1}$ and $189 \pm 10 \text{ cm}^2 \text{ V}^{-1} \text{ s}^{-1}$, respectively, as shown in **Fig. 5c**. The mobilities are the highest among crystals measured, which should be attribute to the record low trap density in these bulk crystals. We notice that the hole and electron mobility ratio is comparable to the mobility-lifetime product ratio, indicating the electrons and holes should have similar recombination lifetimes.

It is worth mentioning that these excellent $\text{FA}_{0.9}\text{Cs}_{0.1}\text{PbBr}_3$ crystals with extremely low defect density were grown from low-purity precursor materials (98% PbBr_2), because the crystallization in solution itself is a purification process. Therefore, the solution method does not need extra energy-consuming purification processes for the precursor materials like the melting methods³⁶. In addition, the as-grown crystals are very transparent, and do not need another zone-refining process³⁷. All of these contribute to a dramatically manufacturing cost decrease. The synthesis of $\text{FA}_{0.9}\text{Cs}_{0.1}\text{PbBr}_3$ crystals is highly producible. Most of as-synthesized crystals are very transparent, clear, and crack-free appearance. Moreover, over 65% of those crystals showed good γ -ray spectral performance. The distribution of γ -ray spectrum energy resolution measured by $\text{FA}_{0.9}\text{Cs}_{0.1}\text{PbBr}_3$ crystals are much narrower than those obtained by FAPbBr_3 and CsPbBr_3 , as shown in **Fig. 5d** and **Fig. S13**.

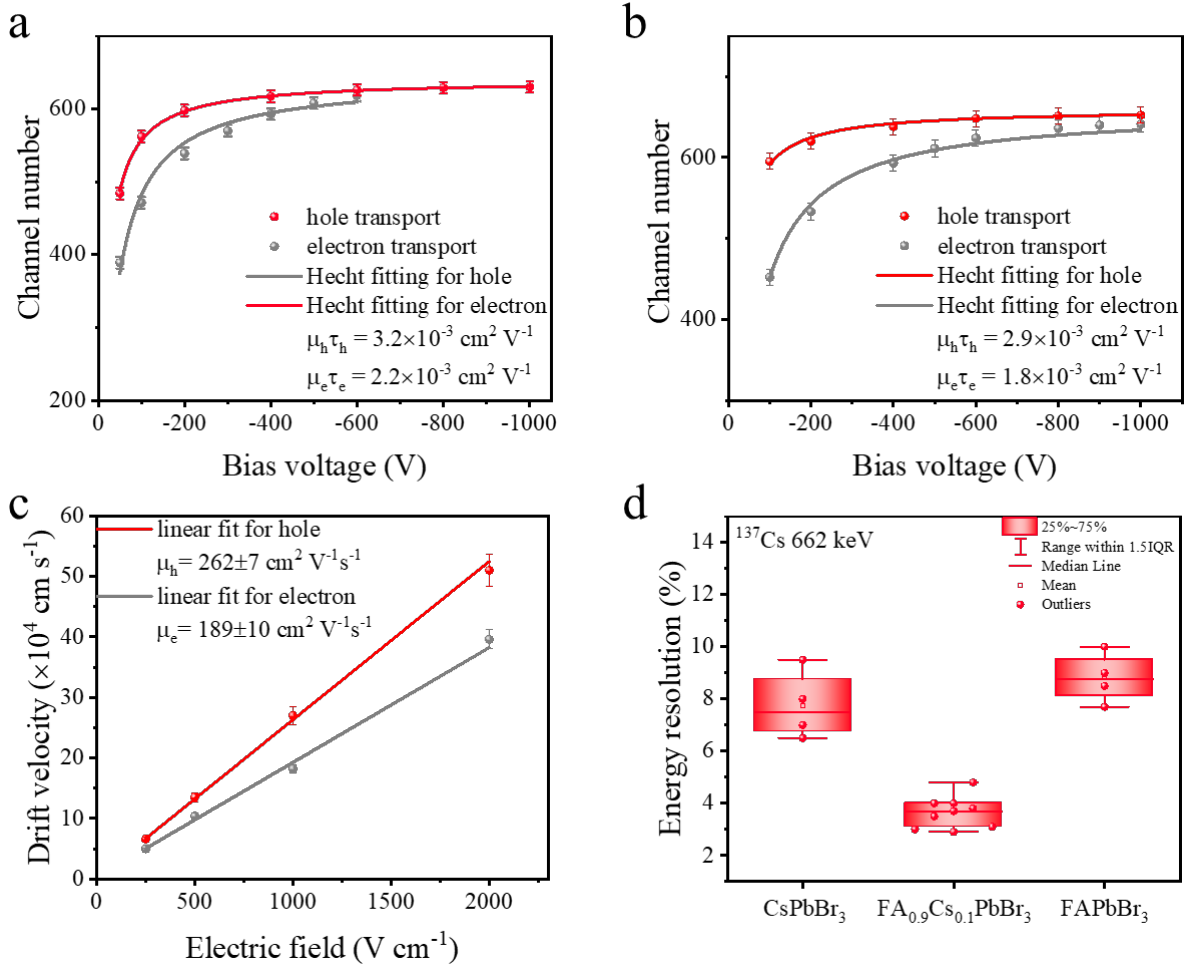


Fig. 5 Optoelectronic properties of FACsPbBr₃ crystals. **a**, The hole and electron mobility-lifetime product fitting for channel number of ^{57}Co 122keV photopeaks under different biases according to Hecht equation. **b**, The hole and electron mobility-lifetime product fitting for channel number of α -particle 5.5MeV photopeaks under different biases according to Hecht equation. **c**, Hole and electron mobility calculation based on voltage-dependent rising time by the ToF technique **d**, Energy resolution distribution of CsPbBr₃, FA_{0.9}Cs_{0.1}PbBr₃, and FAPbBr₃ devices.

In conclusion, we reported high-quality perovskite FACsPbBr₃ single crystals grown by a low-cost solution method. Centimeter-sized clear FA-rich FACsPbBr₃ single crystals were synthesized at high yield due to the elimination of phase transitions when the materials were cooled down from growth temperature to room temperature. The crystal quality is not sensitive to the purity of the raw materials, which should reduce manufacturing cost by at least 10 times than the

melting methods. Surprisingly, FACsPbBr₃ detectors acquired well-resolved spectrums of 59.5 keV ²⁴¹Am, 122 keV ⁵⁷Co, 662 keV ¹³⁷Cs γ -rays and 5.5 MeV α -particle with the best energy resolution of 2.9%. The excellent γ -ray spectral performance can be attributed to the large resistivity ($\sim 9.5 \times 10^9 \Omega \text{ cm}$), high carrier mobility-lifetime products ($\mu_{\text{h}}\tau_{\text{h}} = 3.2 \times 10^{-3} \text{ cm}^2 \text{ V}^{-1}$ and $\mu_{\text{e}}\tau_{\text{e}} = 2.2 \times 10^{-3} \text{ cm}^2 \text{ V}^{-1}$) and a low record low density of charge traps of $\sim 5.6 \times 10^{10} \text{ cm}^{-3}$. FACsPbBr₃ detectors demonstrated remarkable long-term operation and shelf stability, keeping stable response under large biases, and having no degradation over 7 months. The high-performance, low-cost, stable FACsPbBr₃ crystals are very promising candidates as room-temperature radiation detectors with broad applications.

Acknowledgements

This work is financially supported in part by University of North Carolina at Chapel Hill and the Defense Threat Reduction Agency under Award No. HDTRA1-20-2-0002. We thank Dr. Paul Sellin at the University of Surrey for the insightful discussion.

Author contributions

J.H. conceived and supervised the project. L.Z. and Y.L. synthesized crystals. L.Z. fabricated the devices and measured electrical properties and γ -ray spectral performance. Y.Z. built up γ -ray testing system and measured PL, and TRPL. Z.S. contributed to XRD analysis. Z.Y. carried out the DLCP measurement.

Competing financial interests

The authors declare no competing financial interests.

References

1. Johns, P. M. & Nino, J. C. Room temperature semiconductor detectors for nuclear security. *J. Appl. Phys.* **126**, 040902 (2019).
2. Knoll, G. F. *Radiation detection and measurement*. (John Wiley, 2010).
3. Chen, H. *et al.* Development of large-volume high-performance monolithic CZT radiation detector. in *Hard X-Ray, Gamma-Ray, and Neutron Detector Physics XX* vol. 10762 25 (SPIE, 2018).
4. Sajjad, M., Kleppinger, J. W. & Mandal, K. C. Crystal growth, characterization, and fabrication of $\text{Cd}_{0.9}\text{Zn}_{0.1}\text{Te}$ monolithic pixelated detectors for high-energy gamma-ray. in *Hard X-Ray, Gamma-Ray, and Neutron Detector Physics XXI* vol. 11114 276–287 (SPIE, 2019).
5. Kozlov, V., Kemell, M., Vehkamäki, M. & Leskelä, M. Degradation effects in TlBr single crystals under prolonged bias voltage. *Nucl. Instrum. Methods Phys. Res. Sect. Accel. Spectrometers Detect. Assoc. Equip.* **576**, 10–14 (2007).
6. Baciak, J. E. & He, Z. Comparison of 5 and 10 mm thick HgI_2 pixelated γ -ray spectrometers. *Nucl. Instrum. Methods Phys. Res. Sect. Accel. Spectrometers Detect. Assoc. Equip.* **505**, 191–194 (2003).
7. Commercialization of the Rapid-Production Growth Method for Affordable Cadmium Zinc Telluride (CZT) Semiconductor | SBIR.gov. <https://www.sbir.gov/sbirsearch/detail/1640503>.
8. Chen, S. *et al.* Stabilizing perovskite-substrate interfaces for high-performance perovskite modules. *Science* **373**, 902–907 (2021).
9. Wang, Q. *et al.* Efficient sky-blue perovskite light-emitting diodes via photoluminescence enhancement. *Nat. Commun.* **10**, 5633 (2019).

10. García de Arquer, F. P., Armin, A., Meredith, P. & Sargent, E. H. Solution-processed semiconductors for next-generation photodetectors. *Nat. Rev. Mater.* **2**, 1–17 (2017).
11. Wei, H. & Huang, J. Halide lead perovskites for ionizing radiation detection. *Nat. Commun.* **10**, 1066 (2019).
12. Wei, H. *et al.* Dopant compensation in alloyed $\text{CH}_3\text{NH}_3\text{PbBr}_{3-x}\text{Cl}_x$ perovskite single crystals for gamma-ray spectroscopy. *Nat. Mater.* **16**, 826–833 (2017).
13. He, Y. *et al.* CsPbBr_3 perovskite detectors with 1.4% energy resolution for high-energy γ -rays. *Nat. Photonics* **15**, 36–42 (2021).
14. He, Y. *et al.* Resolving the Energy of γ -Ray Photons with MAPbI_3 Single Crystals. *ACS Photonics* **5**, 4132–4138 (2018).
15. He, Y. *et al.* High spectral resolution of gamma-rays at room temperature by perovskite CsPbBr_3 single crystals. *Nat. Commun.* **9**, 1609 (2018).
16. He, Y. *et al.* Demonstration of Energy-Resolved γ -Ray Detection at Room Temperature by the CsPbCl_3 Perovskite Semiconductor. *J. Am. Chem. Soc.* **143**, 2068–2077 (2021).
17. Yakunin, S. *et al.* Detection of gamma photons using solution-grown single crystals of hybrid lead halide perovskites. *Nat. Photonics* **10**, 585–589 (2016).
18. Dong, Q. *et al.* Electron-hole diffusion lengths $>175 \mu\text{m}$ in solution-grown $\text{CH}_3\text{NH}_3\text{PbI}_3$ single crystals. *Science* **347**, 967–970 (2015).
19. Saidaminov, M. I. *et al.* High-quality bulk hybrid perovskite single crystals within minutes by inverse temperature crystallization. *Nat. Commun.* **6**, 7586 (2015).
20. Feng, Y. *et al.* Low defects density CsPbBr_3 single crystals grown by an additive assisted method for gamma-ray detection. *J. Mater. Chem. C* **8**, 11360–11368 (2020).

21. Pan, L., Feng, Y., Kandlakunta, P., Huang, J. & Cao, L. R. Performance of Perovskite CsPbBr₃ Single Crystal Detector for Gamma-Ray Detection. *IEEE Trans. Nucl. Sci.* **67**, 443–449 (2020).
22. Liu, Y. *et al.* Ligand assisted growth of perovskite single crystals with low defect density. *Nat. Commun.* **12**, 1686 (2021).
23. Yu, J. *et al.* Perovskite CsPbBr₃ crystals: growth and applications. *J. Mater. Chem. C* **8**, 6326–6341 (2020).
24. Mozur, E. M. *et al.* Cesium Substitution Disrupts Concerted Cation Dynamics in Formamidinium Hybrid Perovskites. *Chem. Mater.* **32**, 6266–6277 (2020).
25. Noh, J. H., Im, S. H., Heo, J. H., Mandal, T. N. & Seok, S. I. Chemical Management for Colorful, Efficient, and Stable Inorganic–Organic Hybrid Nanostructured Solar Cells. *Nano Lett.* **13**, 1764–1769 (2013).
26. Jin, H. *et al.* It’s a trap! On the nature of localised states and charge trapping in lead halide perovskites. *Mater. Horiz.* **7**, 397–410 (2020).
27. Yin, W.-J., Shi, T. & Yan, Y. Unique Properties of Halide Perovskites as Possible Origins of the Superior Solar Cell Performance. *Adv. Mater.* **26**, 4653–4658 (2014).
28. Ni, Z. *et al.* Evolution of defects during the degradation of metal halide perovskite solar cells under reverse bias and illumination. *Nat. Energy* **7**, 65–73 (2022).
29. Ni, Z. *et al.* Resolving spatial and energetic distributions of trap states in metal halide perovskite solar cells. *Science* **367**, 1352–1358 (2020).
30. Kang, J. & Wang, L.-W. High Defect Tolerance in Lead Halide Perovskite CsPbBr₃. *J. Phys. Chem. Lett.* **8**, 489–493 (2017).

31. Liu, X. *et al.* Solution-Grown Formamidinium Hybrid Perovskite (FAPbBr₃) Single Crystals for α -Particle and γ -Ray Detection at Room Temperature. *ACS Appl. Mater. Interfaces* **13**, 15383–15390 (2021).
32. Pan, W. *et al.* Cs₂AgBiBr₆ single-crystal X-ray detectors with a low detection limit. *Nat. Photonics* **11**, 726–732 (2017).
33. Matz, R. & Weidner, M. Charge collection efficiency and space charge formation in CdTe gamma and X-ray detectors. *Nucl. Instrum. Methods Phys. Res. Sect. Accel. Spectrometers Detect. Assoc. Equip.* **406**, 287–298 (1998).
34. Sellin, P. J., Davies, A. W., Lohstroh, A., Ozsan, M. E. & Parkin, J. Drift mobility and mobility-lifetime products in CdTe:Cl grown by the travelling heater method. *IEEE Trans. Nucl. Sci.* **52**, 3074–3078 (2005).
35. Pan, L., Feng, Y., Huang, J. & Cao, L. R. Comparison of Zr, Bi, Ti, and Ga as Metal Contacts in Inorganic Perovskite CsPbBr₃ Gamma-Ray Detector. *IEEE Trans. Nucl. Sci.* **67**, 2255–2262 (2020).
36. Zappettini, A. *et al.* Growth and Characterization of CZT Crystals by the Vertical Bridgman Method for X-Ray Detector Applications. *IEEE Trans. Nucl. Sci.* **58**, 2352–2356 (2011).
37. Lin, W. *et al.* Purification and Improved Nuclear Radiation Detection of Tl₆SI₄ Semiconductor. *Cryst. Growth Des.* **19**, 4738–4744 (2019).

Methods

Materials.

Low purity Lead Bromide (>98%), Dimethylformamide (DMF, 99.8%), Dimethyl Sulfoxide (DMSO, >99.9%), Gamma Butyrolactone (GBL, \geq 99%), and 3-(Decyldimethylammonio)

propanesulfonate inner salt (DPSI) were purchased from Sigma-Aldrich. Formamidinium Bromide (>99.99%) was purchased from GreatCell Solar. Cesium Bromide (99.9%) was purchased from Alfa Aesar. All raw materials and solvent were used as received without further purification.

Crystal growth by solution method.

For FAPbBr₃, 1.4M precursor solution was prepared by dissolving FABr and PbBr₂ with a stoichiometric ratio of 1:1 in a mixed solvent (DMF:GBL = 1:1 v/v). Upon constant stirring at room temperature for 12 hours, the salts were completely reacted to produce a clear FAPbBr₃ precursor solution. The solution was filtered using a Poly Tetra Fluoro Ethylene (PTFE) filter with 0.2 μm pore size. Then, 10 ml filtered solution was placed in a small glass beaker, and a tiny seed crystal was placed at the bottom center of this beaker carefully. One piece of glass was put on top of the beaker to reduce evaporation rate. We placed them on a hotplate at 40 °C for 2 hours, and slowly increased the temperature at a rate of 2 °C per day. After several days, centimeter sized crystals can be grown from solution.

For CsPbBr₃, 0.9M precursor solution was prepared by dissolving CsBr and PbBr₂ with a ratio of 1:2 in DMSO, which was stirred at 60 °C for 12 hours. 0.3M DPSI was added to the solution and stirred for 3 hours. Then, the solution was filtered using PTFE with 0.2 μm pore size. 10 ml filtered solution was placed in a small glass beaker, and a tiny seed crystal was placed at the bottom center of this beaker carefully. One piece of glass was put on top of the beaker to reduce evaporation rate. We placed them on a hotplate at 70 °C for ~10 hours, and slowly increased the temperature at a rate of 2 °C per day. After several days, centimeter sized crystals can be grown from solution.

For FA_xCs_{1-x}PbBr₃, filtered 1.4M FAPbBr₃ and 0.9M CsPbBr₃ precursor solution were mixed at the molar ratio of x:1-x. Then, the mixed solution was filtered using PTFE with 0.2 μm pore size. 10 ml filtered solution was placed in a small glass beaker, and a tiny seed crystal was placed at the bottom center of this beaker carefully. One piece of glass was put on top of the beaker to reduce evaporation rate. We placed them on a hotplate at 40-60 °C for ~10 hours, and slowly increased the temperature at a rate of 2 °C per day. After several days, centimeter sized crystals can be grown from solution.

Detector fabrication.

As-grown crystal surfaces were fine polished mechanically with 3M polishing papers (400-8000 grits). The residues on the polished surface were washed away by Toluene. Then, crystals are dried in nitrogen flow. 80-nm-thick Au and Bi was deposited on crystal top and bottom surfaces by thermal evaporation. Masks are used for form pixel electrodes. The electrodes were connected by Au wire to the outer electric circuit.

General properties characterization

The X-ray diffraction (XRD) was characterized by Rigaku MiniFlex X-ray diffractometer.

The steady-state and time resolved photoluminescence measurement was conducted with a PicoQuant FT300 spectrometer. A 405 nm pulsed laser with a repetition rate of 0.5-20 MHz was applied.

Optoelectronic properties and γ -ray spectral performance measurement.

The I - V curves were measured by Keithley 2400 source-meter under dark condition, where the resistivity was calculated in the bias of -100V. Dark current stability test was conducted with a sampling rate of 10s per point.

For detector spectroscopic performance measurement, we used $0.8\mu\text{Ci } ^{241}\text{Am}$ 59.5 keV, $1\mu\text{Ci } ^{57}\text{Co}$ 122 keV, and $5\mu\text{Ci } ^{137}\text{Cs}$ 662 keV as the γ -ray sources. As-prepared detectors were put in an Aluminum box to shield noise, which is connected to a charge sensitive amplifier (EV-550, Kromek). The high bias voltage is through EV-550 and applied on the detector. The Shaping amplifier (572A, AMETEK) and Multichannel Analyzer (EASY-MCA 8k) were applied to signal processing and γ -ray spectrum generation. The shaping time used in spectrum measurement is 1 μs .

The mobility-lifetime product $\mu\tau$ was estimated by fitting with Hecht equation: $\eta = \frac{Q}{Q_0} = \mu\tau \frac{V}{L^2} (1 - e^{-\frac{L^2}{\mu\tau V}})$, where η is the charge collection efficiency (CCE), Q and Q_0 are the maximum and theoretical saturated channel number of photopeak/shoulder, respectively. V is the bias and L is the detector's thickness.

The mobility μ was calculated by recording pulse height using oscilloscope. We used the average rising time under different biases to get the mobility according to this equation: $\mu = \frac{V_{dr}}{E} = \frac{L^2}{V \times t_{dr}}$. where V_{dr} is the drift velocity, E is the electric field, V is the applied bias, L is the device's thickness, and t_{dr} is the carrier drift time.

For the DLCP measurements, the DC bias (V) was scanning from 0 V to the 40V for the single crystal detectors. While AC bias (δV) was ranging from 20 to 200 mV. The capacitance measured at each δV was recorded and fitted with a polynomial function $C = C_0 + C_1\delta V + C_2(\delta V)^2 + \dots$ to obtain C_0 and C_1 . With the determination of C_0 and C_1 , the total carrier density (N) that includes both free carrier density and trap density at the profiling distance X from the junction barrier is calculated by $N = -\frac{C_0^3}{2q\epsilon C_1 A^2}$, where q is the elementary charge, ϵ is the dielectric constant of the semiconductor and A is the active area of the junction. The profiling distance from the junction barrier was calculated by $\frac{\epsilon A}{C_0}$, which was changed by tuning the V . For each ac bias, an additional offset dc voltage was applied to keep the maximum forward bias constant. The trap density within a certain trap depth range was calculated by subtracting the total carrier density measured at a larger E_ω (lower AC frequency) with that measured at a smaller E_ω (higher AC frequency).

Supplementary Files

This is a list of supplementary files associated with this preprint. Click to download.

- [FACsPbBr3SupplementaryinformationLiangZhao.docx](#)